Simulation of surface deposits of micron sand particles in the internal cooling duct with a Gaussian probability density model

Shihong Xin[1,2] · Kuahai Yu[1,2] · Xindong Xu[1,2] · Shile Yao[1,2] · Hangyu Wang[1]

Abstract

Fine particles of ash and sand can deposit on the surfaces of cooling ducts, diminishing heat transfer efficiency and threatening the operation of turbine engines. The surface roughness of deposits can alter the nearby flow dynamics, and result in changes of subsequent particle collision and deposition. In this work, the effects of rib turbulence on particle deposition in cooling duct are numerically studied based on the wall modeled shear stress transport k–ω model with a UDF code correction for particle–wall impacts and the discrete particle model. A Gaussian probability density function is adopted to give the topology of deposited particles on the surface impacted by micron particles. We investigate how variables such as particle diameter and temperature impact collision and deposition processes. Additionally, the impact of ribbed turbulence on particle deposition is also discussed. The findings indicate that the impact ratio increases with particle diameter while exhibiting less sensitivity to temperature. Deposition ratios experience a significant decrease when particle size exceeds 1 μm. The temperature of the particles has a noteworthy influence on surface profile of deposits. Specifically, deposits on the wall surface, where particles are introduced by fluid injection, tend to assume a crane-like shape as the temperature rises. Notably, a more uniform deposition pattern is achieved when the particle temperature is low. In terms of particle distribution, low-velocity particles are more likely to accumulate in the windward region of the rib, especially at the junction of the rib wall, where the maximum deposition height is observed. Furthermore, deposits on the rib surface tend to grow, and the gap between the peak and valley widens as the particle temperature increases, as evident from the roughened rib surface features.

1 Introduction

In environments like deserts or when flying through volcanic ash clouds, gas turbines are susceptible to ingesting a significant quantity of fine particulates, including ash, sand, and dust particles smaller than 10 μm. Despite the presence of advanced filtration and cleanup systems, some of these fine particles become heated by the hot gas and collide with the outer surface of turbine blades, resulting in erosion, corrosion, and deposition. Additionally, numerous particles enter the cooling supply system, adhering to the inner surfaces of cooling ducts. While external deposition may provide a level

of protection due to its low thermal conductivity, safeguarding the component from the hot gas, it is important to note that when particles deposit on the internal surfaces of cooling ducts, such as by clogging film holes, the components become exposed to higher temperatures. This exposure can lead to a deterioration in cooling performance and localized thermal damage to the blade metal [1].

The behavior of particle collision and deposition within cooling ducts is influenced by a multitude of parameters, rendering it more complex than the deposition on the outer surfaces of turbine blades. To gain a comprehensive understanding, controlled laboratory-based experimental measurements of particulate transport and deposition have been conducted. The Turbine Accelerated Deposition Facility (TADF) operates under high-temperature conditions, facilitating the exploration of particle deposition mechanisms during extended operational periods [2–4]. Results from these experiments reveal that the rate of particle deposition is contingent on factors such as particle material [5],

✉ Kuahai Yu
yukuahai@163.com

1 Department of Engineering Mechanics, Henan University of Science and Technology, Luoyang, China

2 Particulate and Multiphase Flow Science International Joint Laboratory of Henan Province, Luoyang, China

particle and gas temperatures [6], particle size, and surface temperature [7], among others. The interplay of these factors collectively shapes the particle collision and deposition behavior within cooling ducts, introducing further complexity.

Furthermore, the analysis extends to the thickness, structure, and surface roughness of deposits generated within the accelerated deposition facility. This investigation seeks to elucidate the mechanisms governing the evolution of deposition [8], resulting in the creation of three-dimensional maps illustrating the roughened surfaces caused by deposits [9]. In parallel, a low-temperature and low-speed deposition experiment platform, operating on the principles of similarity, has been adopted to simulate deposition processes, offering energy-efficient and cost-effective means of study [10, 11].

An experimental study involving the deposition of melted Paraffin has revealed that Paraffin deposits undergo initial growth until they reach a state of equilibrium thickness [12]. It has also been observed that the deposition of particles is influenced by the surface roughness of the coupon [13]. The formation and accumulation of these deposits result in surface roughening, altering the roughness and topology of the affected surfaces. This, in turn, has a significant impact on the nearby fluid field and heat transfer efficiency. The role of deposit roughness cannot be underestimated [14].

Understanding the mechanisms behind deposit evolution is of paramount importance, and a comprehensive study is highly desirable. However, the complexity and high costs associated with facility tests make them challenging to undertake, even though they hold the key to a deeper understanding of deposition mechanisms. In the quest to predict the deposition of micron-sized particles on turbine blades, various collision and deposition theories and models have been put forth. The prospect of these deposition theories have significantly advanced the field of numerical prediction for deposition processes. The commercial software fluent is widely used by researchers due to its strong capability in gas–solid two phases simulation.

Tafti [15] developed a critical viscosity deposition model to predict the deposition of sand particles under high-temperature conditions. This model links the probability of sand particle deposition to its viscosity, which is determined by temperature. Using the critical viscosity model, Tafti and colleagues explored erosion and deposition of sand particles within a short pin fin array [16] and discussed the characteristics of particle deposition in cooling ducts [17, 18]. Subsequently, Singh and Tafti further enhanced the critical viscosity model by introducing a soft ball collision mode that accounts for deformation losses during collisions but does not include the influence of temperature [19].

Yu and Tafti devised a physical-based model for particle collision and deposition. This model considers various factors, such as incoming angle, velocity, temperature effects on

material properties, particle rolling and sliding, and energy losses, to determine the coefficient of restitution (COR) and deposition probabilities [20]. However, this model's application in simulations is limited due to the need for numerous parameters to be determined.

Moreover, Yu and Liu developed a simple COR-fitted function for sand particles impacting DD3 nickel-based single crystal surfaces. They used this function to investigate dust transport and accumulation in ribbed cooling ducts [21]. Their research also delved into the collision, adhesion, and deposition of micron-sized dust particles within internal cooling ducts equipped with pin fin arrays [22].

The numerical studies mentioned above overlook the impact of surface roughness resulting from deposits. A study conducted by Marchis et al. demonstrated that near-wall turbulence and subsequent particle dynamics were profoundly influenced by this surface roughness [23]. Research indicates that the coefficient of restitution and the trajectories of subsequent particles are substantially modified due to the presence of deposit structures. To account for the influence of deposition profiles on the flow field, the primary method employed is the dynamic mesh morphing approach, where the flow field is updated based on the volume of deposited particles [24–26].

Zhou et al. utilized a two-dimensional dynamic mesh model in conjunction with computational fluid dynamics (CFD) to investigate the changing shape of ash deposits as they grow on a cooled probe [27]. Despite advances in understanding deposit evolution, much of the work has been conducted in two-dimensional models coupled with the dynamic mesh morphing method due to computational constraints [28, 29]. There has been a limited focus on the surface profile of deposits within a three-dimensional cooling duct.

The numerical studies mentioned above overlook the impact of surface roughness resulting from deposits. A study conducted by Marchis et al. demonstrated that near-wall turbulence and subsequent particle dynamics were profoundly influenced by this surface roughness [23]. Research indicates that the coefficient of restitution and the trajectories of subsequent particles are substantially modified due to the presence of deposit structures. To account for the influence of deposition profiles on the flow field, the primary method employed is the dynamic mesh morphing approach, where the flow field is updated based on the volume of deposited particles [24–26].

Zhou et al. utilized a two-dimensional dynamic mesh model in conjunction with computational fluid dynamics (CFD) to investigate the changing shape of ash deposits as they grow on a cooled probe [27]. Despite advances in understanding deposit evolution, much of the work has been conducted in two-dimensional models coupled with the

dynamic mesh morphing method due to computational constraints [28, 29]. There has been a limited focus on the surface profile of deposits within a three-dimensional cooling duct.

This paper introduces a comprehensive collision and deposition model for micron particles to predict the rebounding and depositing characteristics of particles in the cooling ducts combining with the Gaussian probability density function for describing the morphology of deposits. The primary objective of this study is to examine the deposition behavior of micron-sized sand particles within a three-dimensional ribbed cooling duct under high-temperature conditions. Specifically, our aim is to characterize the deposition profiles on an impingement coupon and the ribbed surface. We will explore the influence of particle size and temperature on collision ratios, deposition ratios, and the resulting deposition profiles. By conducting this comprehensive analysis of fine particle deposition, our findings will contribute to a better understanding and prediction of deposition characteristics in various heat transfer equipment.

2 The methodology of simulation

2.1 Computational methodology

The interaction between the gas and solid phases in the cooling duct is simulated using the Eulerian–Lagrangian technique. The turbulent flow field is modeled with the shear stress transport turbulence model, specifically the k–ω SST variant. It is important to note that the suitability of the k–ω SST model for simulating particle transport has been previously validated in our prior research [21].

The governing equations, which encompass the conservation of mass, momentum, and energy, are applied to model the turbulent airflow are listed as follows:

$$\begin{cases} \dfrac{\partial \rho}{\partial t} + \dfrac{\partial (\rho u_i)}{\partial x_i} = 0 \\ \dfrac{\partial \rho u_i}{\partial t} + \dfrac{\partial (\rho u_i u_j)}{\partial x_j} = -\dfrac{\partial p}{\partial x_i} + \dfrac{\partial}{\partial x_j}\left(\mu \dfrac{\partial u_i}{\partial x_j} - u_i{}' u_j{}' \right) \\ \dfrac{\partial T}{\partial t} + \dfrac{\partial (u_i T)}{\partial x_i} = \dfrac{\partial}{\partial x_i}\left(\dfrac{\lambda}{\rho c_p} \dfrac{\partial T}{\partial x_i} \right) \end{cases}$$
$$(1)$$

where u, p, μ, and ρ are velocity, pressure, dynamic viscosity coefficient, and density of gas, respectively. T, c_p and k are temperature, specific heat capacity and thermal conductivity of gas, respectively.

Particles are simulated in the Lagrangian frame work, each particle is tracked using the law of momentum conservation. The particles undergoing many forces such as drag force F_{drag}, Saffman lift force F_{lift}, thermophoretic force F_{T},

pressure gradient force F_{p} from the flow. The particles are simplified to be spherical and the forces acting on each particle are described as

$$m_{\text{p}} \frac{\mathrm{d} u_{\text{p}}}{\mathrm{d} t} = F_{\text{drag}} + F_{\text{lift}} + F_{\text{P}} + F_{\text{T}} + F_{\text{collision}} \tag{2}$$

where the $F_{\text{collision}}$ is the force operated by the wall when the particle contact wall surface. The micron-sized sand particles are injected uniformly from the inlet, the one-way coupling between flow fluid and particles is adopted ignoring the influence of particle on fluid due to the low volume fraction of particles in the flow.

While tracking the particles within the flow domain, they may encounter a range of forces that lead to interactions with the structural walls. When a particle–wall collision occurs, this section will provide a brief overview of how particle responses, including reflection or deposition, will be described for a comprehensive understanding.

2.2 Particle–wall collision and deposition model

The particle–wall collision and deposition model, which was initially developed and validated in our previous work [20, 21], is now introduced and explained. This model focuses on the energy dissipation occurring during the collision process of micron-sized sand particles with DD3, a nickel-based single crystal superalloy. It provides predictions for both the normal and tangential recovery coefficient (COR) when a particle comes into contact with a wall surface, considering factors such as deformation and adhesion energy dissipation. Utilizing this model, the deposition velocity of the sand particles can be calculated. In this section, we offer a brief overview of the model for the sake of completeness.

2.2.1 Normal collision and deposition

In the context of particle–wall impact, a particle undergoes three distinct stages: the elastic stage, the elastic–plastic stage, and the fully plastic stage, all of which are contingent upon the normal impact velocity of the particle, denoted as V_{ni}. The boundaries between these stages are determined by two critical normal impact velocities, V_{cn} and V_{cpn}, which separate the respective stages. These critical velocities are determined by considering the mechanical properties of both the particle and the wall, as discussed in reference [20].

On the basis of Hertz contact theory, the rebound kinetic energy of the particle W_{nr} is obtained by subtracting the plastic loss from the total kinetic energy of the particle W_{ni}. The particle size and temperature effect on the mechanical properties as yield stress and Young's modulus of sand grains

were considered in this model.

$$W_{\mathrm{ni}} = \frac{1}{2}mV_{\mathrm{ni}}^2 \quad W_{\mathrm{nr}} = \frac{8}{15}E_*R_*^{1/2}\delta_{\mathrm{rc}}^{5/2} \tag{3}$$

where δ_{rc} is the recovery deformation, E_* and R_* are the equivalent elastic modulus and equivalent radius, respectively.

In addition to accounting for the energy loss due to plastic deformation of particles and surfaces, we also consider the absorption of energy resulting from adhesion forces (denoted as W_{A}) and the dissipation of energy due to surface asperities (referred to as W_{asp}). These elements are detailed in the following equations:

$$W_{\mathrm{A}} = \Delta\gamma\pi(a_{\mathrm{p}}^2 + a_{\mathrm{c}}^2/2^{4/3}) \tag{4}$$

$$W_{\mathrm{asp}} = \frac{1}{24}\pi^2 a_{\mathrm{max}}^2 r_{\mathrm{asp}}\sigma_{\mathrm{asp}} \tag{5}$$

where the $\Delta\gamma$, $a_{\mathrm{c}}, a_{\mathrm{p}}$ are the surface energy per unit area, the critical contact radius between elastic and elastic–plastic stage, and the plastic contact radius, respectively.

The σ_{asp} was the yield strength of the wall material, respectively. The r_{asp} is the radius of the surface roughness.

The normal recovery coefficient e_{n} and the normal recovery velocity can both be calculated out as following equations:

$$\begin{cases} e_{\mathrm{n}} = \sqrt{(W_{\mathrm{RF}} - W_{\mathrm{A}} - W_{\mathrm{asp}})/W_{\mathrm{ni}}} \\ V_{\mathrm{nr}} = e_{\mathrm{n}}V_{\mathrm{ni}} \end{cases} \tag{6}$$

This indicates that particles will adhere or deposit on the surface when the normal rebounding coefficient (e_{n}) becomes zero, signifying a balance between the energy losses due to adhesion force (W_{A}) and the surface plastic energy (W_{asp}) with the normal rebound kinetic energy. It is at this equilibrium point that the critical depositing velocity of the particle can be determined.

Based on the composition of sand, the softening temperature of sand ranges from 1000 to 1200 °C. Figure 1 presents representative normal recovery coefficients (e_{n}) with incoming velocities for a range of particle sizes (1–5 µm) at various temperatures. In Fig. 1a, it is evident that the normal coefficient of restitution (COR) initially increases and then decreases with an increase in normal impact velocity. This behavior can be attributed to adhesive forces dominating energy losses in low-velocity impacts, while high-velocity collisions exhibit plastic energy dissipation. Under low-velocity impact conditions, the normal recovery coefficient e_{n} decreases as the particle diameter decreases, primarily due to the more pronounced effect of adhesive forces on smaller particles. Figure 1a also reveals that the normal recovery coefficient e_{n} tends to approach zero when the normal impact

velocity (V_{ni}) falls below a critical value (V_{cr}). This signifies that particle deposition occurs when V_{ni} is less than the critical normal velocity V_{cr}.

Furthermore, as shown in Fig. 1a, the normal critical deposition velocity (V_{cr}) increases as the particle size decreases. The predictions in Fig. 1b indicate that the normal recovery coefficient e_{n} decreases as the temperature rises. This suggests that deposition is more likely to occur for 1 µm sand particles at higher temperatures. Specifically, the values of the normal critical deposition velocity (V_{cr}) for 1 µm sand particles are predicted to be 2.69 m/s, 4.75 m/s, and 10.46 m/s at temperatures of 1273K, 1323K, and 1343K, respectively.

Incorporating the collision and deposition model into a computational fluid dynamics (CFD) simulation can be challenging due to its complexity. To address this issue, we propose an exponential fitting function for the coefficient of restitution (COR) for sand particles when they come into contact with the DD3 wall surface. This function is determined based on parameters such as particle velocity, temperature, and size and is presented as follows:

$$\begin{aligned} \mathrm{COR} = &[1 - 4.296 \times 10^{-4} \times (T - 1073)] \\ &\times (2 \times V_{\mathrm{ni}}^{-0.09035} - 0.8689) \times (d/5)^{-0.1573} \end{aligned} \tag{7}$$

where T, V_{ni}, and d are the Kelvin temperature, normal impact velocity, and diameter of particle, respectively. When the normal velocity of the particle, denoted as V_{ni}, falls below the critical deposition velocity, V_{cr}, the particle adheres to the surface. In contrast, if V_{ni} exceeds V_{cr}, the particle reflects off the surface with a normal velocity magnitude of $V_{\mathrm{ni}} \times$ COR (coefficient of restitution). In this context, deposition is primarily influenced by the normal COR, with the tangential collision effects being disregarded.

2.2.2 Tangential collision

Although the tangential effect on deposition behavior is not considered in present study, the tangential recovery coefficient is of great importance for particle motion in the flow field. A function predicting sand particle tangential rebound or recovery behavior is written as [30]:

$$e_t = 1 - \mu_{\mathrm{s}}\tan\alpha \cdot (1 + e_n) \tag{8}$$

where α is the inclined angle between the particle incidence velocity direction and the wall surface, μ_{s} is the friction coefficient of sliding.

2.3 The surface topology of deposits reconstruction

As particles consistently accumulate on the structure's surface, the roughened deposits impact skin friction and cause
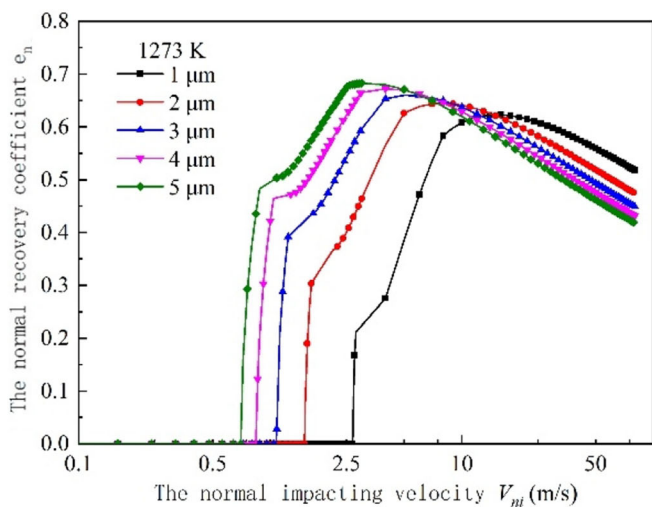
(a) The normal COR of different size particle
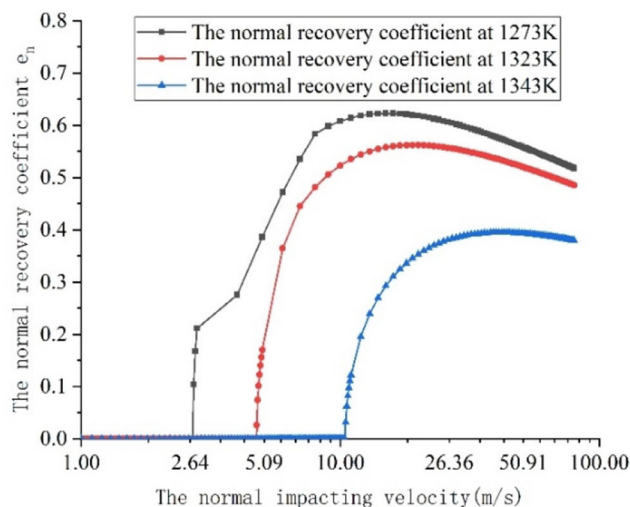
(b) The normal COR of 1μm particle

Fig. 1 Normal recovery coefficient of micron sand particles

variations in convective heat transfer rates [9]. Furthermore, the surface characteristics of these deposits exert a notable influence on the surrounding flow field, altering the collision dynamics for subsequent particles. Therefore, it is essential to develop maps of deposit distributions during the deposition process. This study presents a methodology for generating three-dimensional surface representations of deposits based on the positions of deposited particles and the surface grid.

In Fig. 2, we present a flowchart illustrating the process of generating the surface topology of deposits. As a particle comes into contact with the surface structure, its velocity perpendicular to the surface (V_i) is compared to the critical depositing velocity (V_{cr}). When V_i is less than or equal to V_{cr}, the particle adheres to the surface, and its impact position is recorded. If V_i is greater than V_{cr}, the particle undergoes reflection according to the coefficient of restitution (COR).

At regular intervals, calculations are made to determine the number of particles deposited in each surface grid, followed by a redistribution process based on the Gaussian probability density function. The height of each surface grid is computed by equating it to the total volume of all particles deposited within that specific grid. A construction process is then executed to generate the final map depicting the roughened surface resulting from these deposits. It is worth noting that the effects of deposited particles rolling, tamping, or flaking off have been disregarded in this analysis.

2.3.1 Target meshing

The surface of the coupon, which is exposed to particle impacts, is divided into square cells as illustrated in Fig. 3. To determine the number of particle collisions and depositions in each cell, we calculate this by comparing the particle

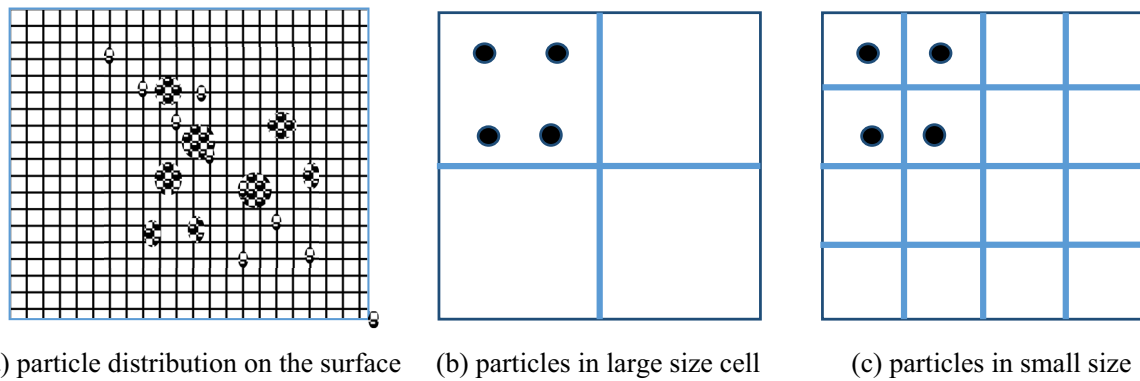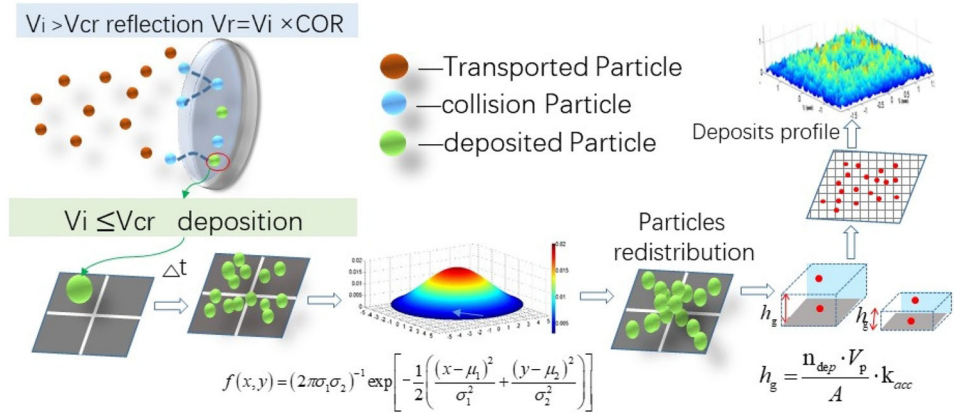coordinates with the coordinates of the cell borders in both the *x* and *y* directions.

Figure 3b, c illustrates that the number of particles within each cell is influenced by the uniform grid size of the target mesh. Consequently, the distribution of deposited particles exhibits significant grid dependence, leading to variations in the surface profile of the deposits. Additionally, it is worth noting that the deposition model employed in this study does not account for the potential rolling and stripping of particles after deposition, nor does it consider how the presence of deposited particles might affect the deposition characteristics of subsequent particles. The roughness of the deposited surface exhibits a degree of randomness that warrants consideration.

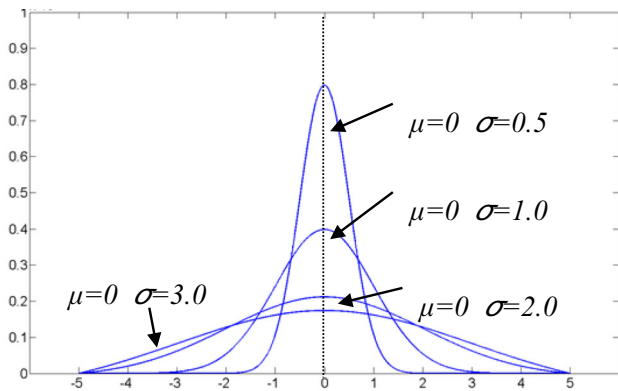### 2.3.2 The Gaussian probability density function

The Gaussian distribution is a valuable tool for representing random variables with uncertain distributions. In fact, the height distribution function of most real surfaces can be approximated quite effectively using a Gaussian distribution [26]. In our current study, we have employed the Gaussian probability density function to model the random roughness of surfaces that have been deposited upon by particles. This function is used to describe the likelihood of particles being displaced (either through rolling or sliding) to adjacent positions or cells on the surface mesh. The one-dimensional distribution function is expressed as follows:

$$f(x) = \left(2\pi\sigma^2\right)^{-\frac{1}{2}} \exp\left[-\frac{1}{2}\frac{(x-\mu)^2}{\sigma^2}\right] \tag{9}$$

Fig. 2 The production flowchart of the roughed surface by deposits

$$f(x,y) = (2\pi\sigma_1\sigma_2)^{-1} \exp\left[-\frac{1}{2}\left(\frac{(x-\mu_1)^2}{\sigma_1^2} + \frac{(y-\mu_2)^2}{\sigma_2^2}\right)\right]$$

(a) particle distribution on the surface   (b) particles in large size cell   (c) particles in small size

Fig. 3 Distribution of deposited particles in the surface cells

Fig. 4 The curve of Gauss probability density function

In determining the axis of symmetry and the steepness of the distribution curve, the parameters μ and σ play a crucial role, as illustrated in Fig. 4. When it comes to the formation and growth of particle deposits on a two-dimensional plate surface, the Gaussian probability density function is adapted or modified as follows:

$$f(x, y) = \left(2\pi\sigma_i\sigma_j\right)^{-\frac{1}{2}} \exp\left[-\frac{1}{2}\left(\frac{(x-\mu_i)^2}{\sigma_i^2} + \frac{(y-\mu_j)^2}{\sigma_j^2}\right)\right] \tag{10}$$

In the given context, the subscripts "i" and "j" represent the x and y directions, respectively. The variables μ_i and μ_j denote the coordinates of the cell center, where the particle is deposited.

Figure 5 illustrates the probability diagram for a particle within one cell moving to surrounding cells with parameters $\mu = 0$ and $\sigma = 3.0$. When a particle deposits on the surface, the cell number where the particle is deposited is recorded. These particles have varying probabilities of moving to one of the five nearby cells, as dictated by Function 10. The information presented in Fig. 5 suggests that when a particle is deposited in one cell, it is likely to either roll or slide to neighboring cells, in accordance with the probability distribution described in Function 10. The probability of movement increases as the distance between the center of the cell, where the particle is deposited and the centers of the surrounding cells, decreases. To capture the randomness of particle deposition on the surface, all the particles within each cell are redistributed using a Gaussian probability density function, as defined by Function 10.
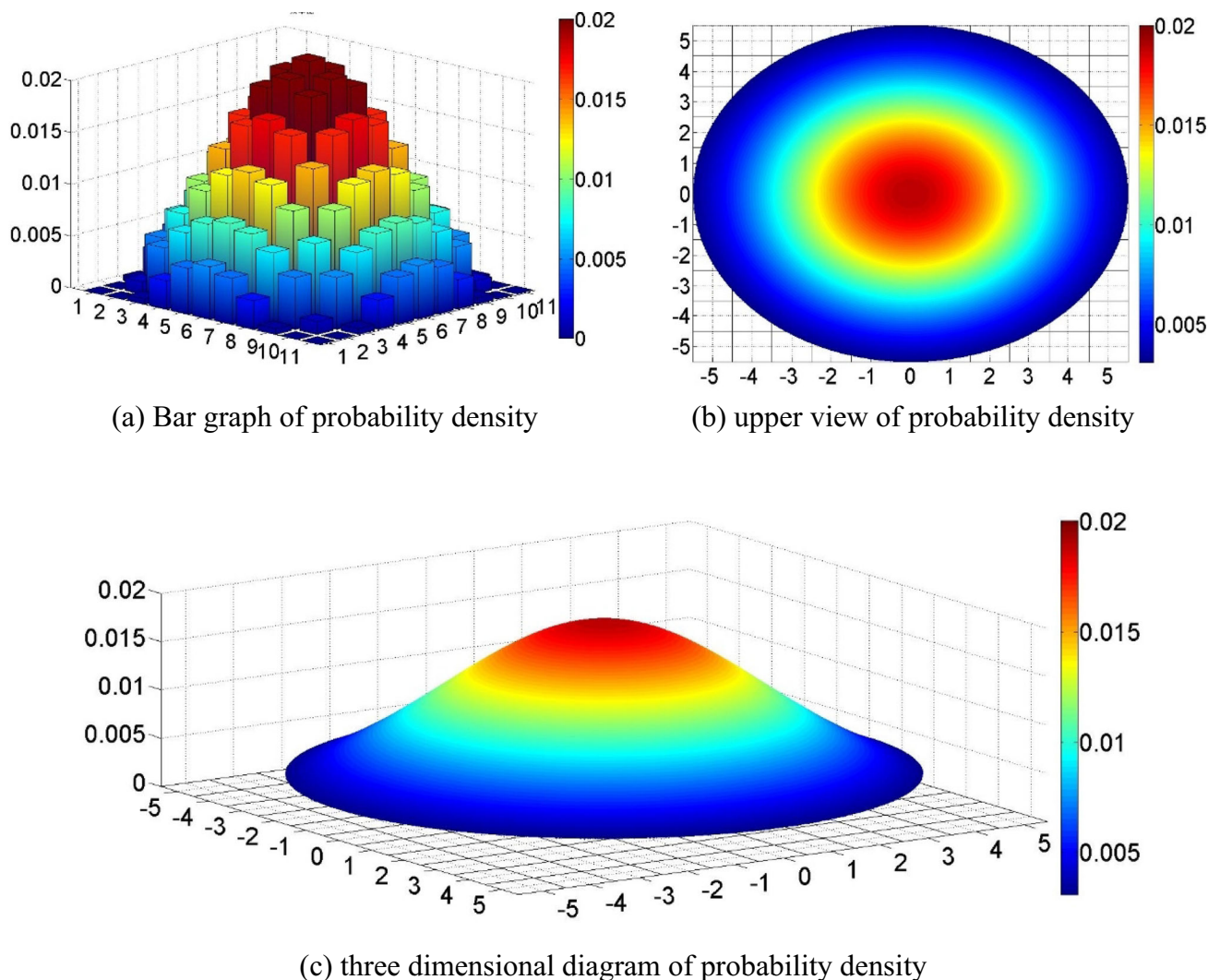
(a) Bar graph of probability density

(b) upper view of probability density

(c) three dimensional diagram of probability density

Fig. 5 The distribution of probability density

2.3.3 The height of deposition layer

Once all particles within each surface cell are redistributed according to the Gaussian probability density function, we calculate the total number of particles deposited in each individual cell. In addition to the cell size, the height of each grid, representing the thickness of the deposits, is determined by the total volume of deposited particles. This is accomplished using the volume equivalence methodology, where the height of deposits in each cell is determined according to the following function:

$$h_{\mathrm{g}} = \frac{n_{\mathrm{dep}} \cdot V_{\mathrm{p}}}{A} \cdot k_{\mathrm{acc}} \tag{11}$$

The equivalent height of deposits for each grid (h_{g}) is calculated as the product of the deposited particle number (n_{dep}) and the individual particle volume (V_{p}), divided by the grid

area (A). In the following sections, the h_{g} for each mesh call will be denoted as the average nominal deposition height. To expedite the deposition process and simulate hundreds or thousands of hours under real engineering conditions, we utilize the parameter K_{acc}. The K_{acc} is determined by the equation as $K_{\mathrm{acc}} = \frac{t_{\mathrm{actual}}}{t_{\mathrm{simulation}}}$, where t_{actual} and $t_{\mathrm{simulation}}$ are the actual deposition time in real engine operation or experiments and the total calculation time in simulation, respectively. Ultimately, we create a three-dimensional representation of the surface topography of deposits on the wall surface. This is achieved through a process of smoothing and interpolation, taking into account the equivalent height of deposits in each grid.
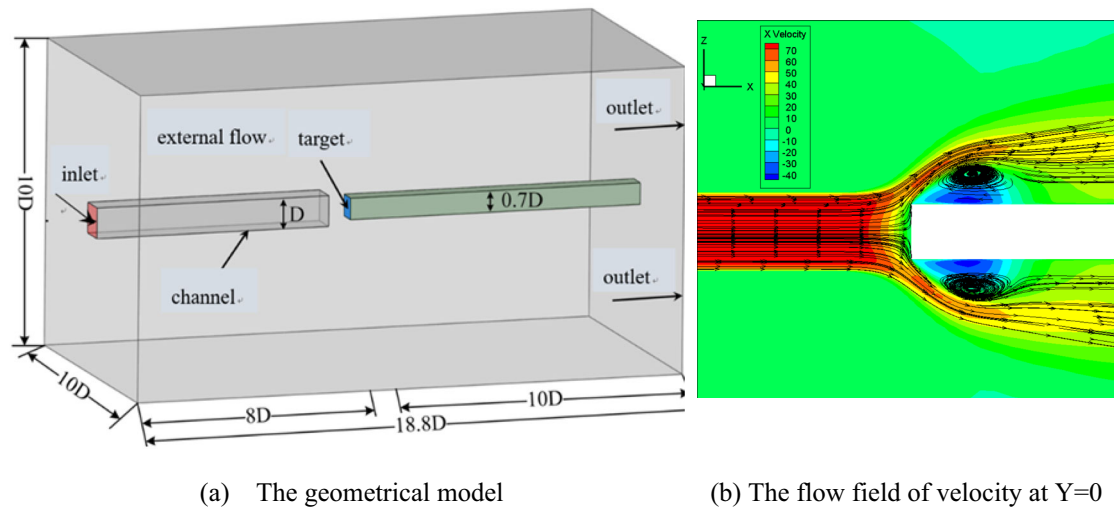
(a) The geometrical model

(b) The flow field of velocity at Y=0

Fig. 6 The impingent jet model

3 Particle deposition on surface under impingent jet

3.1 Model description

Figure 6a gives the geometrical model of the impingent jet, a plane coupon is normally impacted by the air flow mixed with micron sand particles. The inlet tube has a square cross-section with side *D* and length *8D*. The square-sectional target plate has the side *0.7 D* and length *10D*. The computational domain has the size of *18.8D* in length which is along with the stream-wise direction. The length of the domain in other two directions are both *10D*. The target surface center is in line with the axial of the inlet tube, so that particles impact the target normally. The density of cooling air is 8.8 kg/m^3, and the viscosity coefficient is 8.49×10^{-5} m^2/s, the operating pressure of inlet is 2.0265 MPa, the convergence residuals is set to be 1×10^{-6} s. Structured grid is used to obtain a high quality mesh. A total number of 3.7 million cells are obtained after the mesh dependency study.

Figure 6b shows the velocity contours in stream-wise direction on the symmetry plane with flow streamlines. The flow velocity is symmetrically distributed. It is seen that a low-velocity region in front of the target and two backflow region near the top and bottom walls of the obstacle behind the target surface. The length of the vortex size is about 1.9 times of the target height which are consistent with the results predicted by Tafti [19], indicating that the turbulent model used here, is reliable.

3.2 Particle collision and deposition on surface

In this case, a total of 200,000 particles are uniformly injected at the inlet surface in 20 consecutive injections, following the attainment of flow field convergence and steadiness. The initial velocity and temperature of the injected particles are set to match those of the surrounding fluid. These particles exit the inlet tube and subsequently impact the target coupon surface. Upon each particle–wall collision, a particle may either reflect from the surface or adhere to it. The determination of whether a particle will deposit or rebound is based on the comparison of the particle's normal velocity, denoted as V_{ni}, with the critical deposition velocity, V_{cr}. Specifically, if V_{ni} is less than or equal to V_{cr}, the particle deposits on the surface. If V_{ni} exceeds V_{cr}, the particle will rebound into the flow, potentially leading to another surface impact or circumnavigating the coupon.

Once deposition occurs, comprehensive data related to each particle, including the number, location, collision time, and velocity information, is meticulously recorded. The terms "collision/impact ratio" (η_{imp}) and "deposition/stick ratio" (η_{dep}) are defined as follows:

$$
\begin{cases}
\eta_{imp} = \dfrac{n_{imp}}{n_{inj}} \\[2mm]
\eta_{dep} = \dfrac{n_{dep}}{n_{imp}}
\end{cases}
\tag{12}
$$

where n_{inj}, n_{imp}, n_{dep} are representing the number of particles injected from the inlet, the number of particles impacted, and the number of particles deposited on the target surface, respectively. To analyze the influence of particle size on collision and deposition, we employ the Stokes number (S_{tp}). The Stokes number is a valuable parameter for estimating how particles respond to airflow. It is defined as follows:
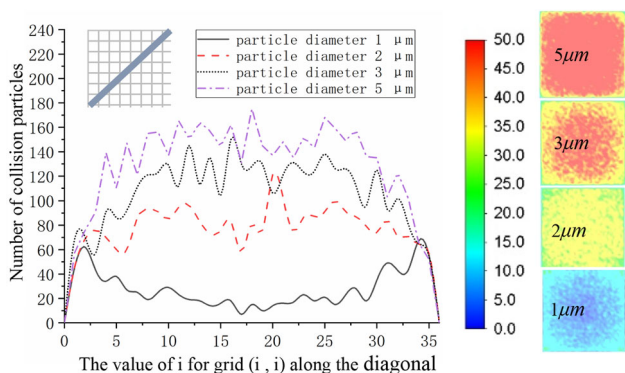
$$
S_{tp} = \frac{\rho_p d_p^2 u}{18 \mu_g L_c}
\tag{13}
$$

Fig. 7 The collision particle number for different size particles

Fig. 8 The deposition for different size particles

Fig. 9 The element coordinate of deposited particles along the diagonal line

In which u, L_c are the velocity and the inlet hydraulic diameter of the airflow, respectively. In the present study, The Stokes number S_{tp} for particle with various diameter as 1 μm, 2 μm, 3 μm, and 5 μm are 0.114, 0.457, 1.029, 1.829, and 2.858, respectively.

Figure 7 illustrates the contours and curves representing particle impingement on the coupon for varying sizes of micron-sized sand particles at a temperature of 1323 K. This figure also provides a comparative analysis of the numerically predicted collision numbers along the diagonal of the square target for particles of different sizes.

It is noteworthy, as observed from the figure, that there is relatively low particle impingement in the center of the coupon, which gradually increases with distance from the center, particularly for 1 μm particles, which have the lowest Stokes number. The Stokes number is a parameter that quantifies how quickly a particle responds to the flow. In the case of 1 μm particles with a Stokes number much less than unity, they tend to closely follow the surrounding flow, resulting in a higher rate of collision in regions farther from the center. The results also indicate that a greater number of particle collisions occur in the center of the coupon when particle sizes range from 2 to 5 μm. As the Stokes number increases, particles tend to impact the coupon's center more perpendicularly due to their higher inertia.

In Fig. 8, we compare the anticipated number of deposited particles on the coupon for the four particle diameters under consideration. The data in Fig. 8 clearly indicate that 1 μm particles exhibit the highest deposition rate, while significantly lower deposition is observed in the other cases. In the case of larger particles, the critical deposition velocity (V_{cr}) is too low to be met in high-velocity flows, resulting in reduced deposition. For the 1 μm particles, the curve along the diagonal of the surface displays a central valley on the coupon with a random distribution of particles. In this central region, a majority of particles tend to move in alignment with the flow, resulting in fewer particle collisions and subsequent deposition.
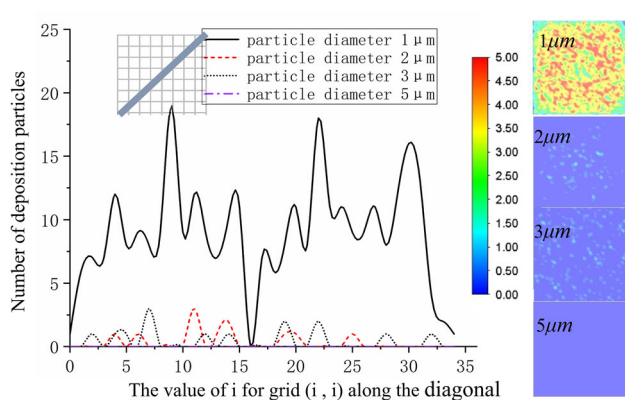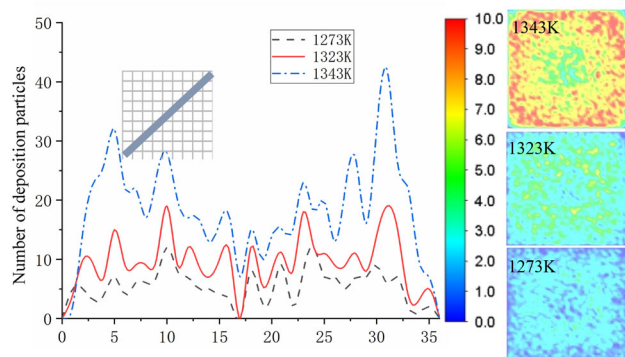
The impact of temperature on deposition is further examined for 1 μm particles, which exhibit a high deposition ratio, as depicted in Fig. 9. The results indicate a direct correlation between deposition and temperature increase. At a temperature of 1343 K, the highest deposition is observed in areas located away from the center of the coupon, highlighting a notable trend. In contrast, a more uniform deposition pattern is evident on the coupon surface as the temperature decreases. This can be attributed to the behavior of particles at higher temperatures; they tend to soften, leading to a faster increase in deposition, particularly in regions away from the center where collisions are more frequent.

In Fig. 10, the impact ratio and deposition ratio are presented for particles of varying diameters, as well as for 1 μm particles at temperatures of 1273 K, 1323 K, and 1343 K. The impact/collision ratio, defined as the number of colliding particles divided by the total number of injected particles, stands at 15.98%, 47.86%, 64.60%, 74.44%, and 78.70% for particle sizes ranging from 1 to 5 μm, respectively.

As illustrated in Fig. 10a, the impact ratio increases with particle size, while the deposition ratio for 2 μm particles experiences a sharp decline when compared to that of 1 μm particles, eventually approaching zero as the particle size

(a) Particle size dependency

(b) Temperature dependency
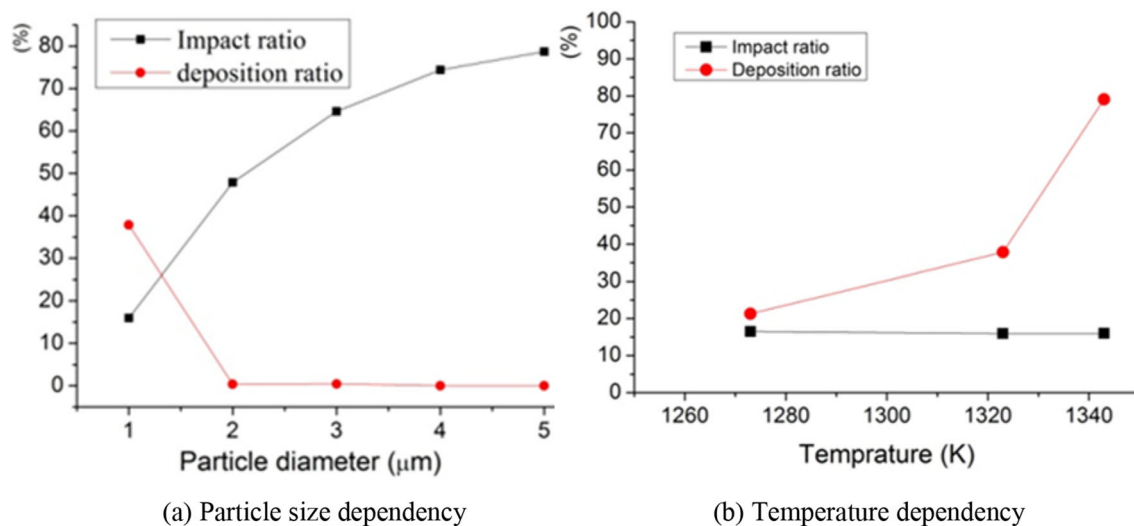
Fig. 10 Impact ratio and deposition ratio for micron sand particles

increases. The deposition ratio, which represents the number of deposited particles divided by the number of colliding particles, for the five different-sized particles is 37.857%, 0.330%, 0.416%, 0.004%, and 0.004%, respectively. This indicates that smaller particles exhibit a greater likelihood of deposition due to their higher critical deposition velocity.

We analyzed the impact of temperature on both the impact ratio and deposition ratio for 1 μm particles at various temperatures, as illustrated in Fig. 10b. The results indicate that the temperature has a negligible impact on the impact ratio, but it does have a notable effect on the deposition ratio. Specifically, as the temperature increases, the deposition ratios correspondingly increase, reaching values of 21.27%, 37.85%, and 79.07%, respectively.

While figure provides deposition information in the form of contours and curves, it lacks the capability to offer a comprehensive view of the surface morphology of the deposits. This limitation restricts our ability to gain a thorough understanding of the surface roughness and the actual height of the deposits. To address this, the following section presents a three-dimensional representation of the surface topology of deposits. This representation specifically focuses on micron-sized sand particles with a diameter of 1 μm. We achieve this by applying a Gaussian probability density distribution in conjunction with the volume equivalence methodology.

3.3 The surface roughness of deposits on plate

When creating a map of surface deposits caused by 1 μm sand particles, it is crucial to account for the grid size of the surface, as this greatly impacts the height of deposits for each individual plane element. Additionally, the parameter variables associated with the Gaussian probability density function can also influence the surface roughness. Figure 11

illustrates the effect of the Gaussian parameter σ on surface roughness. The curves represent the roughness along the axes of the surface deposits, specifically along the symmetry axis at $X = 0$. As σ increases, a milder distribution becomes apparent, and this trend remains consistent when σ surpasses a value of three.

The impact of element size on surface roughness is also investigated, as depicted in Fig. 12. The curves represent the surface roughness at $Y = 0$. It is evident from Fig. 12 that the surface roughness resulting from deposits decreases as the element size increases. As the grid size increases, the surface roughness tends to become smoother.

Roughness parameters such as the average roughness (R_a) and the root mean square roughness (R_{ms}), which effectively convey surface profile information, are employed in this context to characterize the roughness of a surface. These parameters are defined by the following equations:

$$\begin{cases} R_a = \frac{1}{IJ} \sum_{I=0}^{I-1} \sum_{J=0}^{J-1} Z_{IJ} \\ R_{ms} = \sqrt{\frac{1}{IJ} \sum_{I=0}^{I-1} \sum_{J=0}^{J-1} (Z_{IJ} - Z_{mean})} \end{cases} \quad (14)$$

where I and J represent the number of elements along the X and Y directions on the surface, respectively. The Z_{IJ} denotes the height of deposits within each cell. To explore the influence of element size on surface roughness caused by these deposits, Fig. 13 presents a comparison of variations in R_a and R_{ms} concerning the element size and the parameter σ.

In Fig. 13, it is evident that the Ra exhibits little dependence on both cell size and σ, while the R_{ms} decreases as σ and cell size increase. As illustrated in Fig. 13c, the highest

Fig. 11 Construction of surface map using the Gaussian probability density function
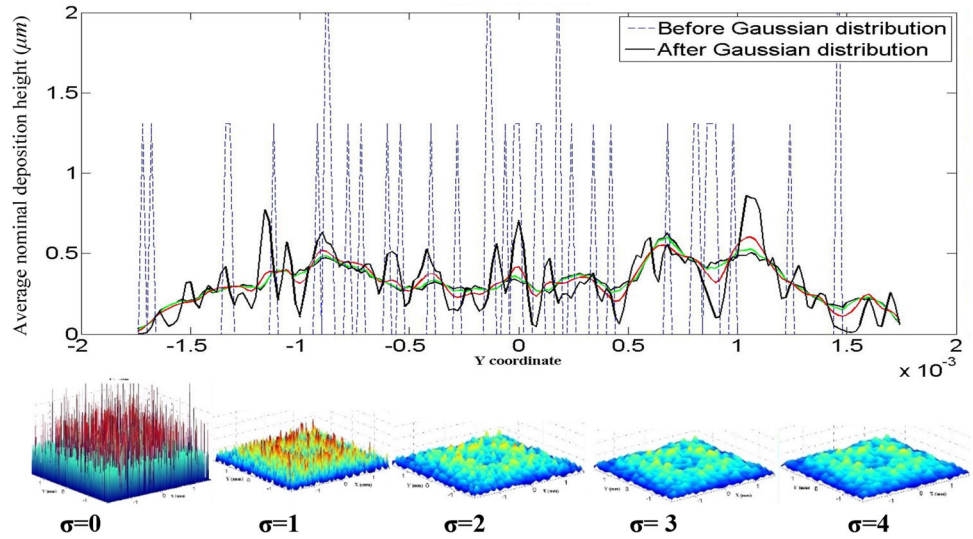
Fig. 12 Surface map of deposits for various grid sizes
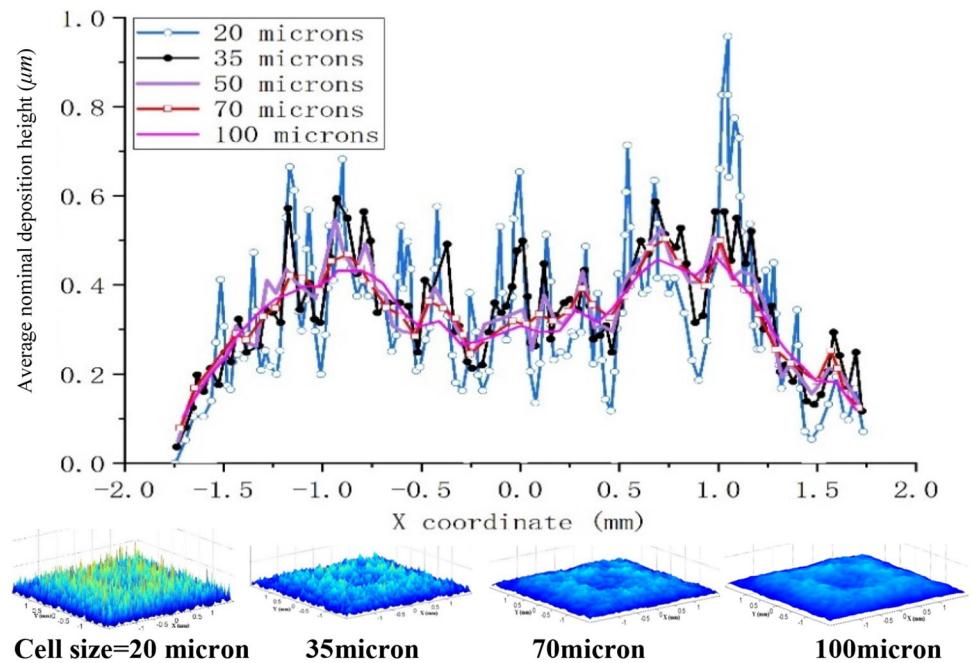
R_{ms} is observed with minimal σ and cell size. However, as σ and cell size increase, R_{ms} tends to decrease and eventually levels off at a constant value. The critical values for σ and cell size are determined to be 3.0 and 50 μm, respectively. Consequently, we have chosen 3.0 and 50 μm for σ and cell size to replicate the surface topography of the deposited coupon particle. It is worth noting that our surface roughness predictions closely align with the experimental results conducted by Wammack [9].

To investigate the influence of temperature on surface roughness due to deposits, Fig. 14 presents predictions of surface roughness at different temperatures: 1273 *K*, 1323 *K*, and 1343 *K*. In Figure (a), it can be observed that both R_a and R_{ms} exhibit minimal change with temperature when the temperature remains below the sand's melting point, which is set to be 1050°. However, when the temperature exceeds 1050°, a significant increase in surface roughness becomes evident. This increase is attributed to the melting of micron-sized sand particles, making them more prone to deposition on the surface. On the coupon surface, a symmetric distribution of deposit roughness is observed.

In Figure (b) and (c), it is evident that deposits tend to grow more prominently in the edge regions as opposed to the center as the temperature increases. Under high temperatures, a deep valley in surface roughness emerges, while a more uniform distribution is observed at lower temperatures. This difference is due to the edge area experiencing a higher incidence of particle impingement and deposition under elevated
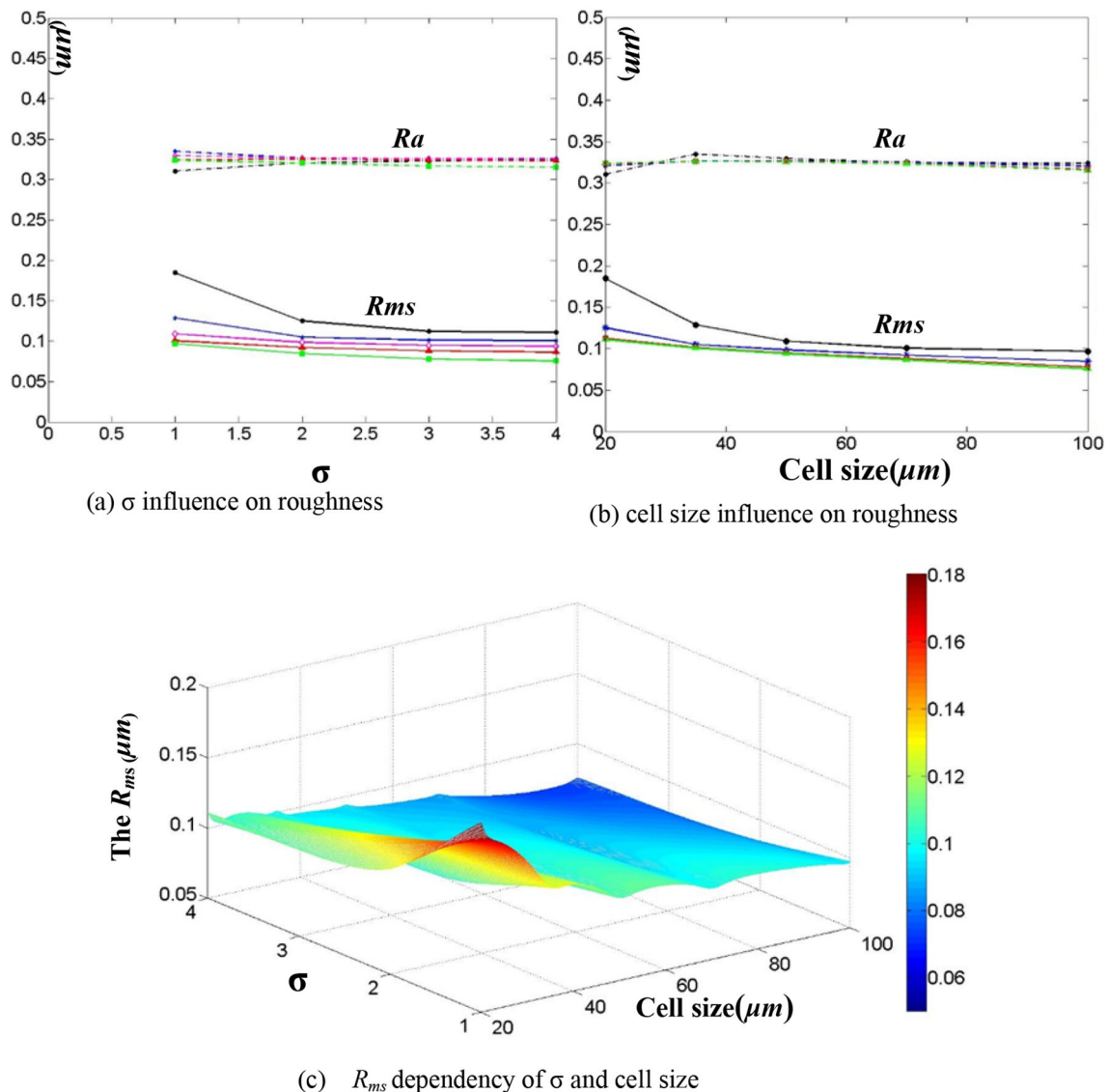
(a) σ influence on roughness

(b) cell size influence on roughness

(c) R_{ms} dependency of σ and cell size

Fig. 13 The parameters of roughness for different mesh sizes

temperature conditions. It is noted that the average nominal deposition height under low-temperature is less than the particle diameter, due to the much short calculation time and low acceleration factor K_{acc} used in the simulation.
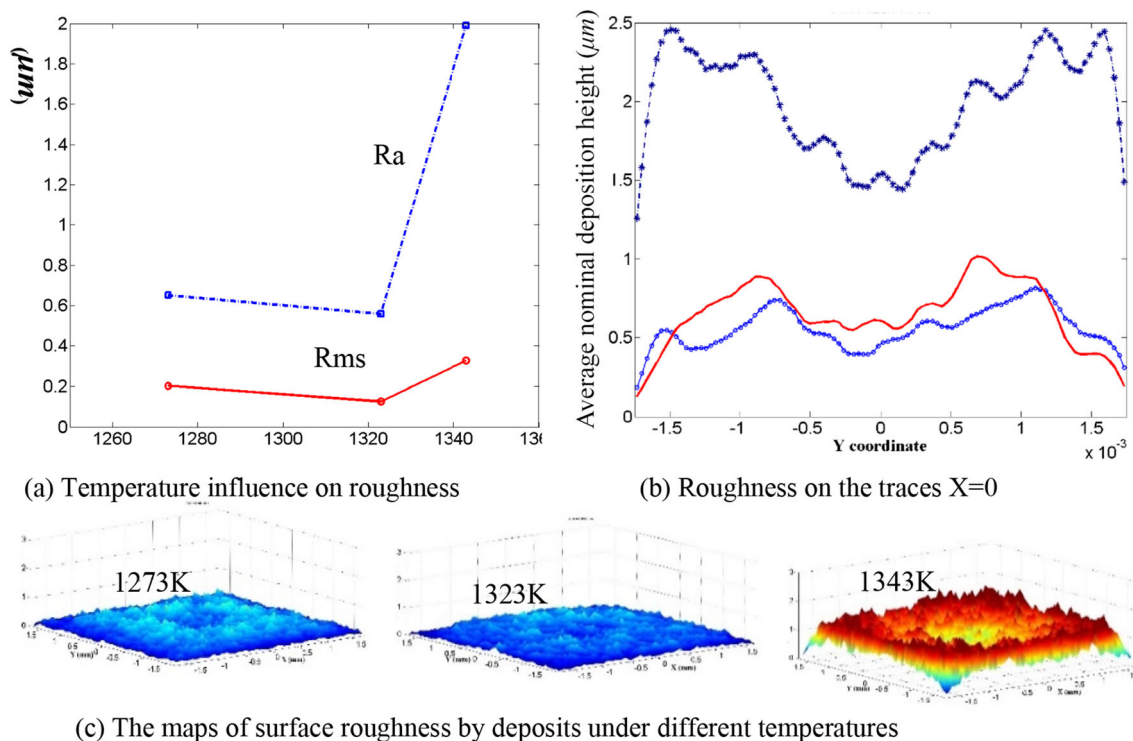
4 Rib effect on deposition

4.1 Model and flow field

The flow dynamics near the walls undergo significant alterations as a consequence of the rib disturbance, which, in turn, leads to an enhancement of heat transfer due to the presence of surface ribs [31]. In this study, we apply a ribbed duct to explore the impact of ribs on particle deposition. Particularly

for particles with diameters less than 5 μm, the forces at play include Vander Waals adhesion forces. When these particles deposit and grow on the ribbed surface, the resulting changes in surface roughness have an influence on adhesion forces, subsequently affecting the deposition process.

For the sake of computational efficiency, a representative periodic single-ribbed duct with a square cross-section is used in our simulation. The geometric and mesh models can be visualized in Fig. 15a, b. The computational domain measures 10 mm × 10 mm × 10 mm, and the ratio of rib length to rib height is 10, with the rib height set at 1 mm. A structured grid is applied, featuring fine grids near all walls, including the rib walls. Following a thorough mesh dependency analysis [21], a total of 2.4 million grid points are employed.

(a) Temperature influence on roughness

(b) Roughness on the traces X=0

(c) The maps of surface roughness by deposits under different temperatures

Fig. 14 The surface deposits morphology under different temperature

A periodic boundary condition is utilized for the outlet. A pressure inlet boundary condition is imposed at 2.0265 MPa, resulting in an average velocity of 167 m/s at the inlet surface. The flow field remains stable until convergence is achieved. In Fig. 15c, the stream-wise velocity pattern with streamlines is depicted on the symmetry plane of the domain at $Y = 5$ mm. Three distinct vortex structures are observed in the flow field, attributable to the rib-induced turbulence. These include a recirculation region behind the rib, a vortex located at the windward region near the rib wall junction, and a smaller recirculation zone on top of the rib.

A total of 200,000 sand particles, each with a diameter of 1 μm, are uniformly injected from the inlet surface. All airflow parameters within the ribbed duct are configured to match those of the impinging jet. In Fig. 15d, a planar view illustrates the distribution of particles along the stream-wise direction within the domain. These particles are represented as points, with low-velocity particles depicted in blue.

The majority of low-velocity particles tend to aggregate in the windward region near the junction of the rib and the surrounding walls. In this region, these particles may undergo secondary collisions with the rib wall or remain suspended in front of the rib for extended periods, which subsequently leads to an increase in particle deposition.

4.2 Particle deposition in ribbed cooling duct

In the context of a gas turbine blade's internal ribbed cooling duct, the ribs are crucial for enhancing heat transfer. However, the accumulation and deposition of particles on the rib surfaces can lead to a reduction in the cooling duct's overall performance, as discussed in reference [18].

Given that particles tend to primarily accumulate and deposit at the junction between the rib and wall, Fig. 16 provides a three-dimensional representation of the surface characteristics of deposits on the windward rib surface and the adjacent up wall at a temperature of 1273 K. For a clearer depiction of the textured deposit surface, the up wall and windward rib surface are flattened into a plane and presented in Fig. 16. The gap between the two curves, which represents the roughness of deposits along the junction line, illustrates that Gaussian redistribution results in a more uniform surface roughness profile. Notably, there are two prominent peaks of deposits observed at the junction between the rib and the surrounding walls, coinciding with the location of recirculation. This suggests that particle deposition is significantly influenced by vortex dynamics, leading to an increase in surface roughness on the nearby surfaces.

In Fig. 17, a comparison is made between the deposit patterns on the upper wall and the windward rib wall surface at varying temperature conditions (1273 K and 1343 K). As depicted in Fig. 17, it is evident that an increase in
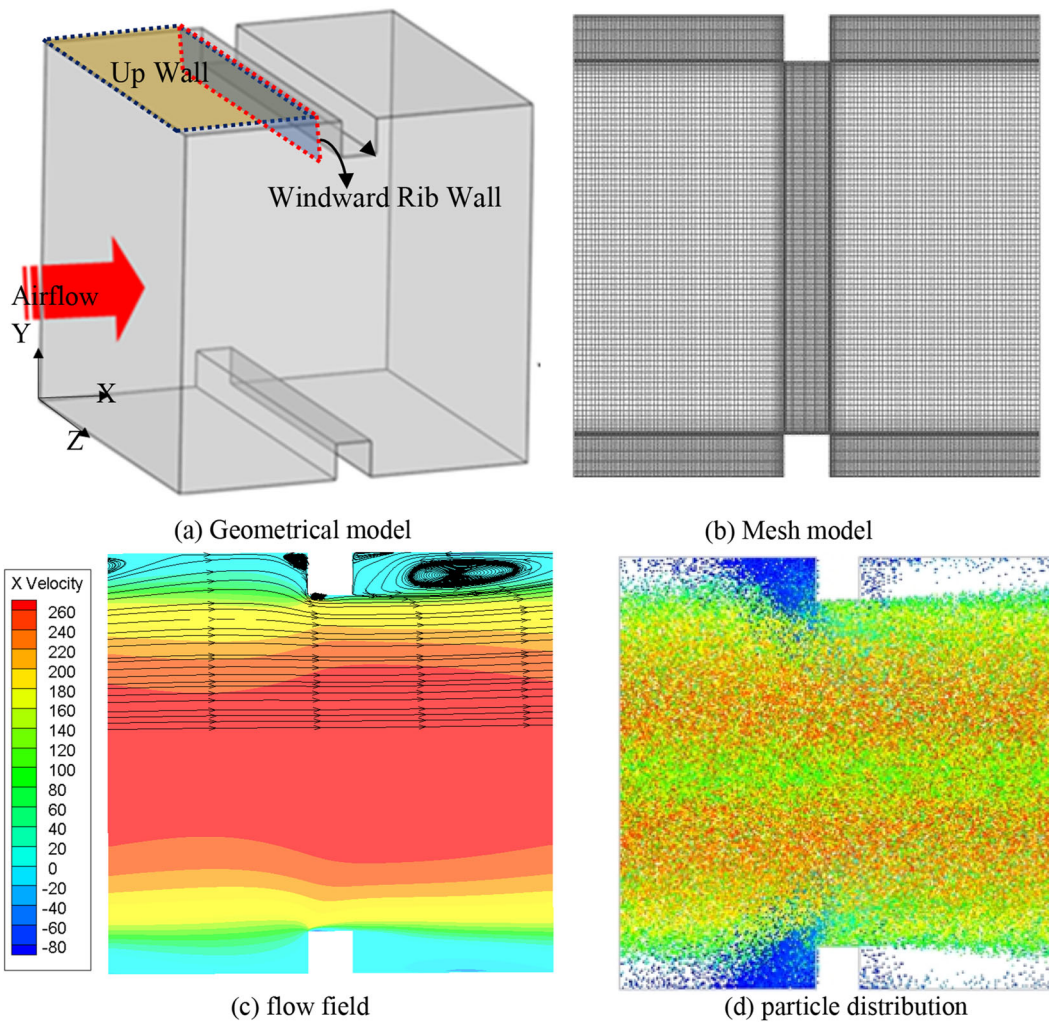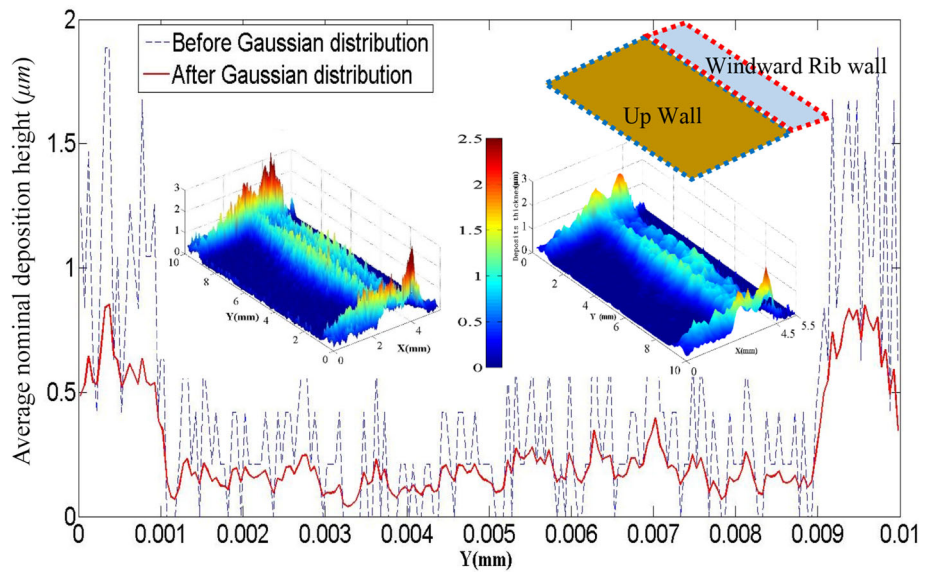
(a) Geometrical model

(b) Mesh model

(c) flow field

(d) particle distribution

Fig. 15 The model of turbine blade ribbed cooling channel

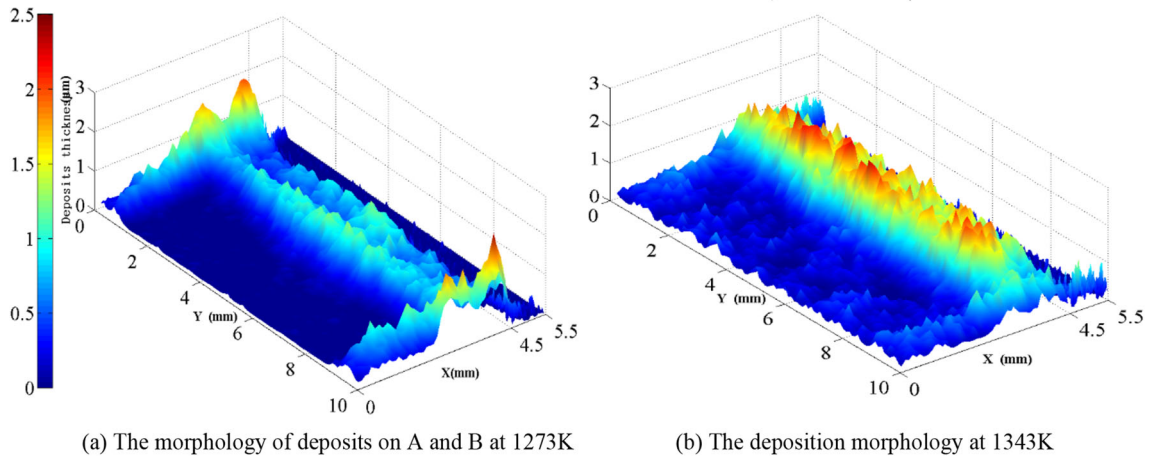**Fig. 16** Particle deposition on the surface of rib wall junction

(a) The morphology of deposits on A and B at 1273K

(b) The deposition morphology at 1343K

Fig. 17 The deposition topography on rib and top wall surface

(a) The roughness of deposits along the junction line A

(b) The roughness on junction line B

(c) The surface roughness of deposits on the windward rib wall
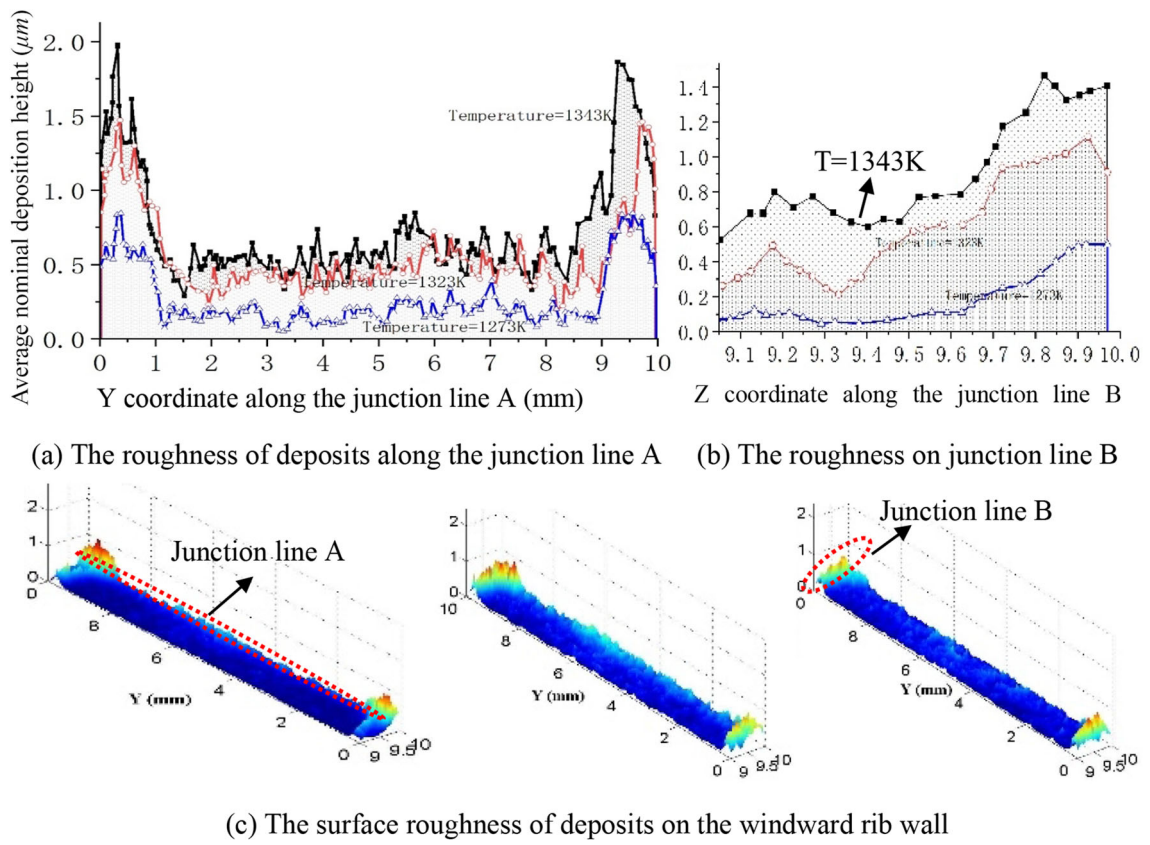
Fig. 18 Particle deposition on the surface of front rib at different temperature

temperature leads to a higher deposition of particles in the central regions of the wall. This can be attributed to the fact that sand particles become more malleable at elevated temperatures, making it easier for them to reach the critical deposition velocity, resulting in increased deposition in the central region. However, the effect of temperature on deposition on the rib surface remains obscured due to the deposits covering the upper wall. To examine the changes

in the shape of deposits on the windward rib wall surface, Fig. 18 illustrates the surface topology of deposits at various temperatures.

In Fig. 18, the curves depicting the roughness of deposits on the windward rib wall are presented along the rib wall junction lines A and B, which are oriented parallel to the rib's length and height, respectively. The peaks of these deposits are notably concentrated at the corners of the rib wall

junction, measuring 0.889 μm, 1.097 μm, and 1.157 μm at temperatures of 1273 K, 1323 K, and 1343 K, respectively. It is worth noting a sharp increase in deposit height at the two ends of the rib wall junction as the temperature rises. This observation indicates that elevated temperatures significantly enhance particle deposition, particularly in the corners of the rib wall junction, where particle accumulation and deposition are influenced by backflow.

Additionally, Figure (b) illustrates a more uniform growth pattern along the rib's height along junction line B as the temperature increases. Higher temperatures lead to an increased presence of low-velocity particles in the rib-surrounding wall junction regions, which are more likely to meet the critical deposition velocity and adhere to the junction surface. This underscores the significant impact of rib turbulence on the transport and deposition of micron-sized sand particles, as it disrupts the flow dynamics.

5 Summary and conclusions

Numerical simulations are conducted to study the collision and deposition of micron-sized sand particles within a cooling duct. The three-dimensional topography of the deposit-roughened surface for both impingent jet and ribbed cooling duct configurations are presented. We also examine the influence of particle size and temperature on particle collision and deposition. Furthermore, we analyze the impact of ribbed turbulence and temperature on deposition within ribbed ducts. The main work and conclusions are listed as follows:

1. A more comprehensive collision and deposition model for micron particles in numerical calculations are adopted to predict the rebounding and depositing characteristics of particles in the cooling ducts. The model considers the effecting factors, such as particle and wall properties, collision velocity, angle, temperature, size, particle rotation and slip, and surface roughness. The coefficient of rebounding for particles is obtained considering energy loss during the collision process. Using this new model. The numerical results show a higher incidence of particle collisions in the central region of the coupon when particles range in size from 2 to 5 μm. Conversely, 1 μm particles exhibit significantly fewer collisions in the central area of the coupon. Notably, the impact ratio increases with an elevated particle Stokes number. 1 μm particles yield the highest deposition ratio, whereas larger particles show less noticeable deposition. The temperature's influence on the impact ratio is minimal, but it leads to a higher deposition ratio as the temperature increases.

2. Based on the random distribution characteristics of rough surfaces, the paper introduces a new method for describing the morphology of deposits using a Gaussian probability density function. The method can predict the three-dimensional morphology of deposits of micron particles in the cooling ducts, especially for long-term deposition, the computation efficiency is increased substantially by multiplying the acceleration coefficient K_{acc}. This will provide a valuable guidance for understanding the depositing process and mechanisms.

3. This paper, based on our own micron particle collision and deposition model combined with a Gaussian probability density distribution function, provides depositing characteristics on rib surface and the effect of rib turbulence on micron particle deposition. It also discusses the impact of particle size and temperature on the distribution pattern of deposits. A crater-like surface morphology is observed at higher temperatures, while lower temperatures result in a more uniform particle distribution. The analysis of micron-sized sand particle deposition within the ribbed duct reveals a clear tendency for particles to predominantly accumulate and deposit in the windward regions, particularly along the rib wall junctions. This behavior is largely influenced by the vortices generated by the rib turbulence. As the temperature rises, there is a pronounced increase in particle deposition at both ends of the rib wall junctions. This is attributed to the backflows, which result in greater particle accumulation and subsequent deposition in these areas.

While we have provided the three-dimensional profiles of surfaces roughened by deposits, our current study does not delve into the impact of surface roughness on the adjacent flow patterns and subsequent particle deposition. This aspect will be thoroughly investigated in future research.

Declarations

Conflict of interest The authors declare that they have no conflict of interest.

References

1. Casaday B, Clum C, Bons JP (2014) Particle deposition in internal cooling cavities of a nozzle guide vane—part II: analytical and computational modeling. In: Proceedings of ASME Turbo Expo, GT2014-27155

2. Prenter R, Ameri A, Bons JP (2016) Deposition on a cooled nozzle guide vane with non-uniform inlet temperatures. J Turbomach 138(10):101005

3. Prenter R, Ameri A, Bons JP (2017) Computational simulation of deposition in a cooled high-pressure turbine stage with hot streaks. J Turbomach 139(9):091005

4. Ai W, Murray N, Fletcher TH et al (2012) Effect of hole spacing on deposition of fine coal fly-ash near film cooling holes. J Turbomach 134(4):041021

5. Webb J, Casaday B, Barker B et al (2012) Coal ash deposition on nozzle guide vanes-part I: experimental characteristics of four coal ash types. J Turbomach 135(1):21033–21033

6. Laycock R, Fletcher TH (2016) Independent effects of surface and gas temperature on coal fly ash deposition in gas turbines at temperatures up to 1400°C. J Eng Gas Turbines Power 138(2):21402.1-21408

7. Crosby JM, Lewis S, Bons JP, Ai W et al (2008) Effects of temperature and particle size on deposition in land based turbines. ASME J Eng Gas Turbines Power 130(9):051503-1–9

8. Jensen JW, Squire SW, Bons JP (2005) Simulated land-based turbine deposits generated in an accelerated deposition facility. ASME J Turbomach 127:462–470

9. Wammack JE, Crosby J, Fletcher D et al (2006) Evolution of surface deposits on a high pressure turbine blade, part i: physical characteristics. In: ASME Turbo Expo, GT2006-91246

10. Lawson SA, Lynch SP, Thole KA (2012) Simulations of multiphase particle deposition on endwall film-cooling. J Turbomach 134(1):11001

11. Lawson SA, Lynch SP, Thole KA (2013) Simulations of multiphase particle deposition on a non-axisymmetric contoured end wall with film-cooling. J Turbomach 135(3):031032

12. Albert JE, Bogard DG (2013) Experimental simulation of contaminant deposition on a film-cooled turbine vane pressure side with a trench. J Turbomach 135(1):51001

13. Yang XJ, Cui MH, Liu ZG (2018) Experimental study on deposition of particulate on plate surface with cooling film (in Chinese). Propuls Technol 39(6):1323–1330

14. Lugundgeen R, Sacco C, Prenter R et al (2016) Temperature effects on nozzle guide vane deposition in a new turbine cascade rig. In: ASME Turbo Expo, GT2016-57560, South Korea

15. Tafti D, Sreedharan S (2010) Composition dependent model for the prediction of syngas ash deposition with application to a leading edge turbine vane. In: Proceedings of ASME Turbo Expo, GT2010-23655

16. Cowan JB, Tafti D, Kohli A (2010) Investigation of sand particle deposition and erosion within a short pin fin array. In: ASME turbo expo: power for land, sea, and air

17. Singh S, Tafti D (2015) Prediction of sand deposition in a two pass internal cooling duct. In: ASME Turbo Expo. Turbine technical conference and exposition

18. Singh S, Tafti D (2016) Prediction of sand transport and deposition in a two-pass internal cooling duct. J Eng Gas Turbines Power 138(7):072606

19. Singh S, Tafti D (2015) Particle deposition model for particulate flows at high temperatures in gas turbine components. Int J Heat Fluid Flow 52:72–83

20. Yu K, Tafti D (2019) Size and temperature dependent collision and deposition model for micron-sized sand particles. J Turbomach Trans ASME 141:031001

21. Yu K, Liu J, Xu X et al (2022) Dust transport investigation in ribbed cooling duct integrating temperature-dependent elastic–plastic particle collision model. Part Sci Technol 40(2):1–11

22. Liu J, Yu K, Tafti D et al (2023) Dust adhesion and deposition behavior in internal cooling duct with pin fins. Int J Therm Sci 184:107943

23. Marchis MD, Milici B, Sardina G et al (2016) Interaction between turbulent structures and particles in roughened channel. Int J Multiph Flow 78:117–131

24. Mu L, Wang S, Zhai Z (2020) Unsteady CFD simulation on ash particle deposition and removal characteristics in tube banks: focusing on particle diameter, flow velocity, and temperature. J Energy Inst 93(4):1481–1494

25. Forsyth P, Gillespie DRH, McGilvray M (2018) Development and applications of a couple deposition dynamic mesh morphing approach for the numerical simulation of gas turbine flows. J Eng Gas Turbines Power Trans ASME 140(2):022603

26. Qu X, Cai X, Zhang M et al (2017) A facile method for simulating randomly rough membrane surface associated with interface behaviors. Appl Surf Sci 427:915–921

27. Zhou H, Zhang K, Li Y et al (2018) Simulation of ash deposition in different furnace temperature with a 2D dynamic mesh model. J Energy Inst. https://doi.org/10.1016/j.joei

28. Zheng Z, Yang W, Yu P et al (2020) Simulating growth of ash deposit in boiler heat exchanger tube based on CFD dynamic mesh technique. Fuel 259:116083

29. Zheng Z, Yang W, Cai Y et al (2020) Dynamic simulation on ash deposition and heat transfer behavior on a staggered tube bundle under high-temperature conditions. Energy 190:116390

30. Han Z, Xu Z, Sun A et al (2019) The deposition characteristics of micron particles in heat exchange pipelines. Appl Therm Eng 158:113732

31. Liou TM, Wang WB, Chang YJ (1995) Holographic interferometry study of spatially periodic heat transfer in a channel with ribs detached from one wall. ASME Trans J Heat Transf 117:32–39